IEEE Control Systems Letters paper presented at
2024 IEEE 63rd Conference on Decision and Control (CDC)
December 16-19, 2024. MiCo, Milan, Italy

Reliability and Lifetime Optimal Control for Electric Vehicle Power Converters

Amin Rezaeizadeh[1] and Silvia Mastellone[1]

***Abstract*— Currently the large scale adoption of Battery Electric Vehicles (BEVs) is limited due to cost, reliability and lifetime considerations. The power converters, and more specifically their semiconductor switching devices, are the second most likely component to fail in a BEV because of the damage caused by the current-induced temperature cycling. In this paper we propose a novel hybrid frequency and time domain control approach that integrates time-domain performance requirements and frequency-domain reliability requirements, based on a frequency model of the damage. The method is applied to control the motor of a BEV and minimize the damage experienced by the power converter.**

I. INTRODUCTION

BEVs hold the potential to offer a sustainable alternative to traditional Internal Combustion Engine Vehicles (ICEVs). Today, major automotive manufacturers are transitioning towards full-electric vehicle lineups. Together with the scientific and technical communities, they face the challenge of advancing the technology for the next generation of automotive power converters and achieve a sustainable and efficient system to encourage widespread BEV adoption [1]–[4]. These challenges become even more critical when considering future Autonomous Mobility-on-Demand (AMoD) services utilizing BEVs, as they demand significant computational and energy resources [5, 6].

Despite their numerous advantages, electric vehicles still fall short in terms of reliability and longevity compared to their combustion engine counterparts. The focus of the present work is to address some of the limiting issues, specifically for the power converter, by defining optimal operation criteria to limit the damage experienced by the semiconductor components. The performance and experienced damage of a power converter depends on the operating conditions of semiconductor devices, which can vary depending on the application and electrical loads. Specifically, the current profile across the semiconductors determine the level of stress and damage experienced. Regulating the current allows to control the level of stress and thus damage experienced.

Responsible system operation contributes to reduce the system long-term damage and to increase the its lifespan. *Reliability Control* realizes this by employing damage models of components and entire systems in the control design phase. For example, in [7] authors model the actuator degradation using a diffusion Wiener process and explore a new type of autonomous maintenance to extend the lifetime of the system. Or in [8], a desired reliability is actively controlled on a slow time scale in order to find a trade-off between reliability and functionality for wind turbine power generation. In [9], authors present an online MPC-based framework that maximizes the lifetime of a multicore real-time system by manipulating core frequencies.

In our previous work [10], we introduced the concept of *Reliability Control*, and proposed an H_∞-control formulation that minimizes the amplitude and frequency of current cycling, thus resulting in a reduced thermal stress and associated damage of the semiconductors. In this work, we propose a hybrid formulation that integrates, in a multi-objective MPC framework, tracking performance requirements encoded as time-domain constraints with reliability requirements encoded as cost function damage in the frequency-domain. The frequency domain formulation allows to use the damage model in an online control policy, without relying on traditional cycle counting.

The control policies, applied to BEV motor control are tested on realistic case studies, where the standard drive cycles speed profiles are tracked by means of the presented control algorithm under realistic load conditions. We illustrate how the online reliability controller can effectively reduced the experienced damage and increase vehicle availability and lifetime without compromising tracking performance.

The paper is structured as follows: Section II describes the model adopted in the control design, including PMSM motor and electro-thermal models of the semiconductor devices that will be used to capture the damage. Section III details the semiconductor characteristics and its losses and damage models in frequency domain used to estimate the device reliability. Section IV present the main result, where the reliability control policy is detailed. The controller performance results are validated in Section V. Section VI is dedicated to concluding remarks and future research directions.

II. SYSTEM MODEL

We consider a BEVs powertrain system as depicted in Figure 1 and consisting of a Permanent Magnet Synchronous Motors (PMSMs) driven by a Silicon Carbite (SiC)-based voltage source converter (VSC) powered by a battery. For the purpose of designing a motor controller that minimizes the damage experienced by the converter, in the following sections we define models for both components.

*This work was supported by NCCR Automation and SNSF

[1]Amin Rezaeizadeh and Silvia Mastellone are with the Institute of Electric Power Systems, University of Applied Science Northwest Switzerland, Windisch-Brugg, Switzerland. amin.rezaeizadeh@fhnw.ch, silvia.mastellone@fhnw.ch

A. Motor model

Within the family of electric motors, permanent magnet synchronous machines (PMSMs) are characterized by higher power density, stable output torque, lower noise level, and good speed regulation performance, making them very suitable for EV propulsion [11].In this work for simplicity we consider a surface-mounted PMSM model where the reluctance torque is neglected and the electrical torque relationship with the current is linear:

$$\tau_{\mathrm{e}} = \frac{3}{2} p \Phi_{\mathrm{F}} i_q(t), \tag{1}$$

where p is the number of pole pairs, Φ_{F} is the constant magnetic flux of the permanent magnet and i_q is the q-component of the motor current.

The angular speed of the motor, $\omega_m(t)$, is governed by the following equation:

$$J\dot{\omega}_m(t) = \tau_{\mathrm{e}} - \tau_{\mathrm{l}} - B_{\mathrm{f}}\omega_{\mathrm{m}}(t), \tag{2}$$

where τ_{l} denotes the load torque, J is the moment of inertia, B_{f} is the viscous friction coefficient, and ω_{m} is the rotor mechanical speed.

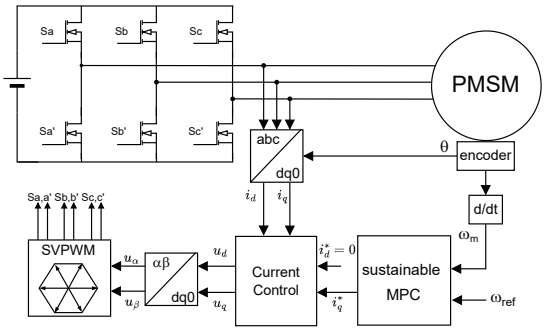

Fig. 1. The PMSM drive system with speed tracking and semiconductors reliability control scheme.

B. Electro-thermal model of semiconductor switches

The motor is powered by the converter current, that produces thermal cycling in the semiconductor switches and increases their junction temperature T_{j}. This temperature variation can be modeled by a series thermal resistance and capacitance network. For simplicity, we only consider the following first order thermal model:

$$C_\theta \dot{T}_{\mathrm{j}}(t) = P(t) - \frac{T_{\mathrm{j}}(t) - T_{\mathrm{a}}}{R_\theta}, \tag{3}$$

where R_θ and C_θ are, respectively, the thermal resistance and capacitance of the semiconductor, $P(t)$ denotes the power loss in the device, and T_{a} is the ambient (heatsink) temperature.

For SiC MOSFET devices, the total average power losses over the switching cycle is given by

$$P \approx r_{\mathrm{on}} I_{Drms}^2 + P_{sw}, \tag{4}$$

where r_{on} is the drain-source on-state resistance, I_{Drms} denotes the rms value of the on-state current, and P_{sw} is the switching loss which for SiC MOSFETs can be negligible compared to the conduction loss.

III. Damage Analysis of power semiconductors

Power semiconductor devices are the second most likely component to fail in a power converter system due to their vulnerability to current-induced thermal stress [12, 13]. The most frequent failure in a semiconductor switch is bond wire lift-off caused by stress cracks due to thermal cycling experienced by the device during operation. As the temperature fluctuates, the mismatch in the thermal expansion coefficients between the aluminium wire and the silicon results in stress at the bond interface. Consequently, the bond wires become disconnected, leading to an open-circuit failure [14, 15].

The number of cycles to failure can be estimated based on a lifetime model. In this work we use the lifetime model adopted by Semikron [16], to evaluate the semiconductor devices reliability. This model considers only degradation of the bond wire connection to the chip, since bond wire lift-off is the dominant cause of failure in power switches. The number of cycles to failure, N_{f}, of the power switches is given by the following modified Coffin-Manson lifetime model:

$$N_{\mathrm{f}} = A_0 . A_1^{\beta} . \Delta T^{\alpha-\beta} . \exp\frac{E_{\mathrm{a}}}{\kappa_{\mathrm{B}} T_j} . \frac{C + {t_{on}}^{\gamma}}{C + 2^{\gamma}} . k_{\mathrm{thick}}, \tag{5}$$

with

$$\beta = \exp\frac{-(\Delta T_j - T_0)}{\lambda},$$

where T_j and ΔT_j are, respectively, the average and magnitude of the junction temperature cycle, and t_{on} is the duration of the cycle. The remaining factors are constant parameters: E_{a} and κ_{B} are, respectively, the activation energy and the Boltzmann constant, k_{thick} is the chip thickness factor, and A_0, A_1, T_0, λ, α, C, γ are empirically obtained constants given in [16].

As the magnitude and average of the temperature cycles increase, the number of cycles to failure decreases. For example, if a SiC MOSFET is subjected to a temperature stress of $\Delta T_j = 40^{\circ}$, it can survive approximately 300k cycles at an average junction temperature of $T_j = 150^{\circ}$ and a duration of $t_{\mathrm{on}} = 10s$. However, at the same temperature and cycle duration, but with a higher temperature stress of $\Delta T_j = 80^{\circ}$, the expected is only about 10k. It can also be seen that as the duration of the temperature cycles, t_{on}, increases, the number of cycles to failure decreases slightly.

The accumulated damage D_{tot} of the semiconductor switch for one cycle of the mission profile can be determined via the Miner rule, originally proposed by Palmgren and Miner [17] as

$$D_{\mathrm{tot}} = \sum_{i=1}^{n} \frac{n_i(S_i)}{N_f(S_i)}, \tag{6}$$

where $n_i(S_i)$ denotes the effective number of cycles at stress level S_i of the the stress history signal, and $N_f(S_i)$ denotes the available number of life-cycles depending on the material characteristics and can be calculated from (5). The lifetime of the power switches can then be computed by multiplying the inverse of D_{tot} with the duration of the

mission profile.

Remark: From the accumulated damage formula we can infer that we can reduce the damage, either by reducing the number of experienced cycles or by increasing the number of lifetime cycles available to the semiconductors.

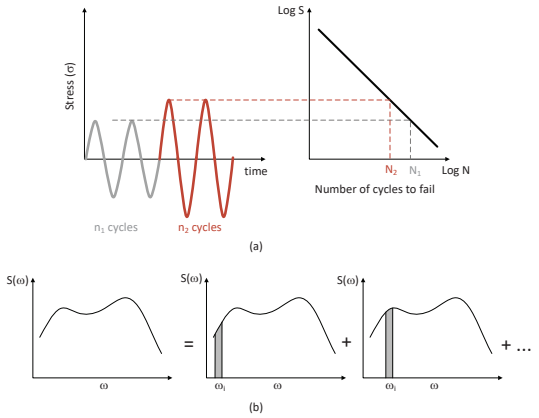

Fig. 2. Fatigue Analysis: (a) Stress versus number-of-cycles-to-failure (the Wöhler-curve or S-N curve), (b) The concept of the single-moment method for damage estimation by decomposing the power spectral density (PSD) of the stress signal into contribution of a set of narrow-band infinitesimal spectrals.

A. Stress and lifetime model: S-N curve

In material fatigue analysis, the S-N curve, introduced by Wöhler, defines the relationship between the applied stress cycle and the number of cycles to failure for a specific material (see Figure 2a). This relationship can be described by the following exponential equation, commonly known as Basquin's equation:

$$N_f = c_{sn} S^{-k_{sn}}, \tag{7}$$

where c_{sn} and k_{sn} are, respectively, the fatigue strength and slope of the S-N curve.

Comparing the Basquin's damage model with the model described by (5) for semiconductor switches, the power law relationship approximately holds for the temperature swing ΔT_j but not for the other two stress factors, i.e., the average temperature and the cycle duration. In the following we will work under the realistic assumption that the temperature variation is the dominant stress factor and neglect the effect of the other two factors variation on the number of available life-cycles and hence on the damage.

B. Damage estimation in frequency-domain

The damage formula defined in (6), requires the knowledge of the effective number of cycles $n_i(S_i)$ at stress level S_i. This is obtained by counting cycles of different stress level in the stress history. In practice cycle counting algorithms, such as the Rainflow [18], are employed. As an alternative to those traditional time-domain nonlinear approaches, spectral methods in frequency domain are employed to estimate $n_i(S_i)$ and thus fatigue damage without the drawbacks of counting algorithms such as computational complexity.

In this work, we will employ the frequency domain based "single moment" method described in [19] to model the damage. This method considers the stress load signal as a uniaxial stochastic process, and estimates the fatigue induced damage as a sum of damage contributions of narrow-band processes, defined by decomposing the original power spectrum in to infinitesimal narrow-band PSDs with bandwidth of $\Delta\omega$ (see Figure 2b). In [20], authors show that, for small values of the S-N exponent ($k_{sn} \sim 3$), the single moment method provide a good approximation of the damage obtained via the Rainflow based time-domain approach for most cases.

Using the single moment spectral approach, the total damage is then computed as

$$D_{\text{tot}} = \left(\sum_{i=1}^{N} D_i^{\frac{2}{k_{\text{sn}}}} \right)^{\frac{k_{\text{sn}}}{2}} \tag{8}$$

where the damage D_i is interpreted as contribution of the infinitesimal power spectrum at around frequency ω_i:

$$D_i = \frac{\omega_i}{2\pi c_{sn}} \left(\sqrt{2S(\omega_i)\Delta\omega} \right)^{k_{\text{sn}}} \Gamma\left(1 + \frac{k_{\text{sn}}}{2}\right), \tag{9}$$

where $S(\omega)$ is the PSD of the stress signal, which in the case of semiconductor damage, would be the temperature signal, and Γ is the gamma function.

IV. Reliability Control Policy

Equipped with the models described in the previous section, we are now ready to formulate the control design problem. The reliability control policy, has the objective to minimize the damage of the semiconductor switches while fulfilling the speed tracking requirement. Using the damage model (8), we define the objective function as

$$J = \sum_{i=1}^{N} D_i^{\frac{2}{k_{\text{sn}}}} \approx \frac{2\Delta\omega \left(\Gamma\left(1 + \frac{k_{\text{sn}}}{2}\right) \right)^{\frac{k_{\text{sn}}}{2}}}{(2\pi c_{sn})^{\frac{k_{\text{sn}}}{2}} N T_s} \sum_{i=1}^{N} \omega_i^{\frac{2}{k_{\text{sn}}}} \left| T(j\omega_i) \right|^2, \tag{10}$$

where the PSD term, $S(\omega_i)$, is approximated by the energy spectral density of the temperature signal. In other words,

$$S(\omega_i) \approx \frac{1}{N T_s} \left| T(j\omega_i) \right|^2, \tag{11}$$

where N denotes the number of frequency bins, which is equivalent to the length of the prediction horizon, and T_s represents the sampling time.

The relationship between junction temperature, $T_j(j\omega)$ and the average power over one switching cycle is given as

$$\begin{aligned} T(j\omega) &= \frac{R_\theta}{1 + j\omega R_\theta C_\theta} P(j\omega) \\ &= \frac{R_\theta}{1 + j\omega R_\theta C_\theta} \frac{r_{\text{on}}}{k_e^2} \mathscr{F}\left\{ \tau_e^2(t) \right\}, \end{aligned} \tag{12}$$

where k_e is the torque constant of the motor.

The discrete Fourier transform (DFT) of the torque-squared profile is given by

$$\mathscr{F}\left\{ \tau_e^2 \right\}_{\omega_i} = \sum_{k=0}^{N-1} \tau_e^2[k] e^{-j\omega_i k T_s}, \tag{13}$$

where $\omega_i = \frac{2\pi}{NT_s}(i-1)$ for $i = 1,2,...N$.

Remark: Minimizing the cost function (10) corresponds to minimizing the H_2-norm of the current profile with a band-pass weight profile defined by the fractional-order band-pass filter defined by the transfer function $G(j\omega)$:

$$G(j\omega) := \frac{(j\omega)^{\frac{1}{k_{sn}}}}{1 + j\omega R_\theta C_\theta}. \tag{14}$$

This filter confines the damping effect of the controller to the thermal bandwidth: current fluctuations at frequencies higher than the thermal bandwidth have minimal impact on the damage, and are therefore discarded. Moreover, low-frequency variations of the current result in fewer cycles. As previously discussed, this spectral representation of fatigue corresponds to an approximation of the Coffin-Manson fatigue model given in (5), in that considers only the variation of the stress signal and neglects the signal bias as a stress factor.

Using the proportionality of the current to the electrical torque, equations (1), the dependency of the temperature on the torque, and omitting the constant terms, equation (12), the cost function defined in (10) can be rewritten as:

$$J(i_q) \propto \sum_{i=1}^{N} |G(j\omega_i)|^2 \left| \mathscr{F}\left\{ i_q^2 \right\}_{\omega_i} \right|^2. \tag{15}$$

A. Receding horizon control

We are now ready to formulate the receding horizon control policy to minimize the damage over a prediction horizon of length N. To better optimize and plan the thermal cycling of the devices over the prediction horizon, we assume that the reference trajectory for the motor speed and the torque load are approximately known at every step for a time interval of the length of the horizon. These assumptions are reasonable in the majority of real-world scenarios. For instance, the adaptation of intelligent speed assistance (ISA) systems into vehicles enables the reference speed to be set automatically according to the path speed limits and the traffic conditions ahead. Furthermore, the load torque can be continuously estimated using the system model parameters.

Since the cost function, defined in (10), is not convex in τ_e, we linearize Eq. (13) at each prediction step by reformulating the torque profile as follows:

$$\begin{aligned} \tau[0] &= \tau_0 + \delta\tau[0] \\ \tau[1] &= \tau[0] + \delta\tau[1] = \tau_0 + \delta\tau[0] + \delta\tau[1] \\ &\vdots \\ \tau[N-1] &= \tau[0] + \sum_{i=0}^{N-1} \delta\tau[i], \end{aligned} \tag{16}$$

where $\tau[k]$ and $\delta\tau[k]$ denote, respectively, the torque profile and its deviation over the prediction horizon, and τ_0 is the the electrical torque, i.e. control variable applied to the motor at the previous step.

With the torque profile decomposed according to (16), the linearized DFT of the torque is given as

$$\mathscr{F}\left\{\tau_e^2\right\}_{\omega_i} \approx \sum_{k=0}^{N-1} \tau_0^2 \left(1 + \frac{2}{\tau_0} \sum_{k'=0}^{k} \delta\tau[k']\right) e^{-j\omega_i k T_s}. \tag{17}$$

Substituting (17) and (12) in (10), and omitting the constant coefficients, the objective function can be rewritten as follows:

$$\begin{aligned} J(\delta\tau) &= \sum_{i=2}^{N/2} \omega_i^{\frac{2}{k_{sn}}} |T(j\omega_i)|^2 \\ &= \sum_{i=2}^{N/2} \omega_i^{\frac{2}{k_{sn}}} \frac{1}{1 + R_\theta^2 C_\theta^2 \omega_i^2} \left| \mathscr{F}\left\{\tau_e^2\right\}_{\omega_i} \right|^2 \end{aligned} \tag{18}$$

Note that the first frequency sample, i.e. $\omega_1 = 0$, is omitted as it does not contribute to the cost.

The amplitude of $\mathscr{F}\left\{\tau_e^2\right\}_{\omega_i \neq 0}$ can be expressed in terms of its real and imaginary parts:

$$\begin{aligned} \left| \mathscr{F}\left\{\tau_e^2\right\}_{\omega_i} \right|^2 &= \Re\left(\mathscr{F}\left\{\tau_e^2\right\}_{\omega_i} \right)^2 + \Im\left(\mathscr{F}\left\{\tau_e^2\right\}_{\omega_i} \right)^2, \\ \Re\left(\mathscr{F}\left\{\tau_e^2\right\}_{\omega_i} \right) &= \frac{2}{\tau_0} \sum_{k=0}^{N-1} \sum_{k'=0}^{k} \delta\tau[k'] \cos(\omega_i k T_s), \\ \Im\left(\mathscr{F}\left\{\tau_e^2\right\}_{\omega_i} \right) &= \frac{2}{\tau_0} \sum_{k=0}^{N-1} \sum_{k'=0}^{k} \delta\tau[k'] \sin(-\omega_i k T_s). \end{aligned} \tag{19}$$

Next we include the speed tracking requirements encoded as constraints. Similar to (16) we define $\omega_m[k]$ to be the speed profile over the prediction horizon. From Eq. (2) the discrete speed dynamic equation is given by:

$$\omega_m[k] = \omega_m[k-1] + \frac{T_s}{J}\left(\tau[k] - \hat{\tau}_l\right), \tag{20}$$

where $\hat{\tau}_l$ is the load torque estimate updated at every time sample.

The speed tracking requirement is then expressed as:

$$|\omega_m[k] - \omega_m^{ref}[k]| \leq \varepsilon \omega_m^{ref}[k], \quad k = 0,...,N-1, \tag{21}$$

where $\omega_m^{ref}[k]$ denotes the required speed profile over the prediction horizon, and ε is a weight that calibrates that degree of flexibility in relaxing the tracking performance requirements to increase the system reliability.

Rewriting the speed according to the expression (20) in (21) leads to the following convex constraint in terms of the torque profile:

$$\begin{aligned} \Bigg| \omega_{m0} + \frac{T_s}{J}\left(k\tau_0 + \sum_{k'=0}^{k-1} k\delta\tau[k'] - k\hat{\tau}_l \right) \\ - \omega_m^{ref}[k-1] \Bigg| \leq \varepsilon \omega_m^{ref}[k-1], \quad k = 1,...,N, \end{aligned} \tag{22}$$

where ω_{m0} is the motor speed measured at the previous time step.

With the reliability objective defined in (18) and the performance constraint as per (22), the optimization problem can be setup as the following QP problem:

Reliability

$$\underset{\delta\tau_e}{\text{minimize}}\ J(\delta\tau_e) \quad \text{subject to} \quad \text{constraint (22).} \tag{23}$$

In the following we refer to *"Reliability Control"* as the control policy designed according to (23), in contrast to *"Performance-oriented Control"*, designed to minimizing the tracking error through the following LP problem:

Performance

$$\underset{\delta\tau_e,\ \varepsilon}{\text{minimize}}\ \varepsilon \quad \text{subject to} \quad \text{constraint (22).} \tag{24}$$

We mention the performance-oriented control design as an extreme case to demonstrate how much the lifetime can be improved by integrating the reliability feature into the control framework and allowing the tracking requirement to vary within a defined limit.

V. Simulation Results

To evaluate the performance of the two control methods, we implement both controller on an automotive drivetrain simulation and run a series of test simulations using the Worldwide harmonized Light vehicles Test Cycles (WLTC) as the reference speed profile (see Fig. 3). This speed profile is frequently used by vehicle manufacturers as a standard driving condition to determine the fuel efficiency and emissions of vehicles. The WLTC driving cycle is composed of four driving phases: urban, suburban, rural and highway, which simulate different speeds ranging from 0 to 140 km/h.

The receding horizon controller updates the current (or torque) reference to the inner loop controller at a rate of 1 Hz. This update rate is sufficient to capture the temperature dynamics with a time constant of 0.45 seconds (Nyquist rate of 0.7 Hz). The number of frequency samples is chosen as N=36, which gives a prediction horizon of length 36 seconds. The average computation time is 1 millisecond, as measured on a Windows PC with an Intel Core i7 1.1GHz processor and 16GB of RAM. The optimization problems are solved using CVXGEN fast QP solver in Matlab [21].

Figure 3 compares the speed tracking performance applying two different control strategies. When employing the performance-oriented controller, the simulated speed closely matches the reference trajectory, with a minimal root mean square error (RMSE) of 0.02 km/h. In contrast, the reliability controller yields a larger speed tracking RMSE of 1.8 km/h, as expected. Figure 4 compares the PSD of the current-squared profiles for the two control strategies. The weight function $G(\omega)$ is also plotted in this figure. The objective of minimizing the total damage, i.e. the area beneath the curve, results in a decrease in the value of damage contribution at some frequencies. Applying the reliability control, the total damage reduces by approximately 60%.

Figure 5 illustrates the resulting current profiles across the entire drive cycle for the two control strategies. Recalling that the accumulated damage is proportional to the temperature fluctuation and hence current fluctuation, the relative damage assessment of the two control strategies can be done by comparing the current profiles. Notably, the reliability control strategy demonstrates reduced torque fluctuations compared to the performance-oriented control. Figure 6 displays the junction temperature of a single SiC MOSFET for each control scenarios. It is evident that the reliability control policy leads to reduced temperature fluctuations. In all the frequency plots we can observe the selective bandpass effect of the reliability control policy. Moreover, recalling the formula of the accumulated damage, we can observe that the reliability control policy reduces the damaging effect of the stress signal by: (i) decreasing the amplitude of the critically damaging stress thermal cycles that correspond to low number of available life-cycles N_f, thus transforming those cycles into less damaging ones with a corresponding higher value of N_f; (ii) reducing the overall number of cycles. To analyse the reliability control policy impact on the MOSFET lifetime, the total damage is calculated using both the spectral method as per (8), and the Rainflow-counting algorithm given in (6), and including the variation of ΔT_j, T_j and t_{on}. Both methods of damage calculation shows a reduction of approximately 60% with the reliability control policy. Thus, under the performance-oriented control action, the SiC MOSFETs are predicted to endure for approximately 5000 drive cycles, which is equivalent to 2500 hours. However, when reliability control is used, the power modules would last for 15,000 drive cycles, or an equivalent of 7600 hours. Since the realistic drive-cycle of a vehicle is different from the WLTC, these lifetime values do not accurately reflect the actual lifetime prediction of the semiconductor switches. Nevertheless, these values provide a useful measure for evaluating different control policies. The performance and reliability metrics are summarized in Table I.

TABLE I

Comparison of the two control strategies.

Quantity \ Control	Performance (24)	Reliability (23)
Tracking RMSE	0.02 km/h	1.8 km/h
Damage (PSD)	-	-62%
Damage (Rainflow)	-	-66%
Battery throughput	2.5 Ah	2.1 Ah

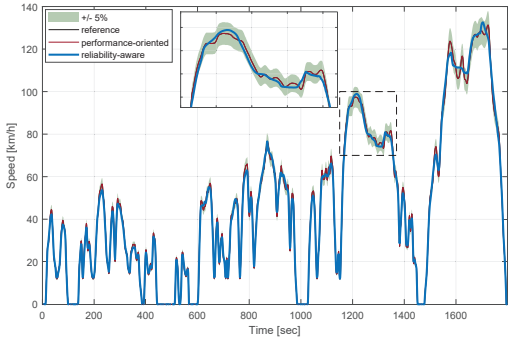

Fig. 3. Speed tracking performance for two different control policies compared to the reference WLTC drive cycle.

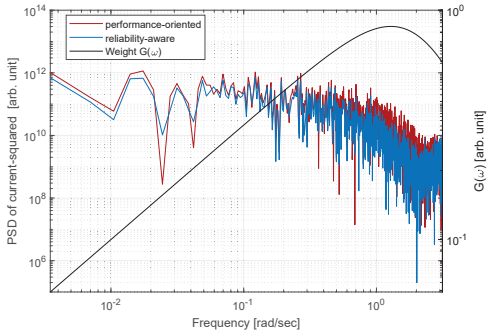

Fig. 4. Comparing the spectrum of damage contribution at different frequencies for both control strategies.

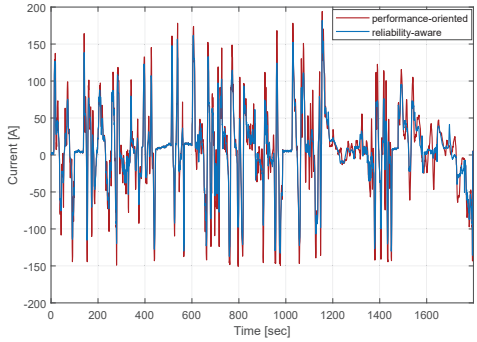

Fig. 5. The resulting current (i_q) profile for the two control strategies.

VI. Conclusion

As for many engineering systems, the control of BEVs power trains focuses traditionally on performance and at best efficiency requirements. This paper employs the concept of reliability control, where the operation of BEVs power converters is optimized to minimize damage, and maximize lifetime, of individual components, i.e. power semiconductor, and of the system, i.e. converter. In particular we proposed a control policy that integrates the tracking and reliability requirements in an hybrid time- and frequency-domain MPC framework that enables to efficiently and reliably operate BEV power converters under varying driving conditions. The proposed approach offers a novel perspective and insights into the sustainable operation of BEVs, paving the way for an entire suite of studies toward a more environmentally aware and reliable automotive future.

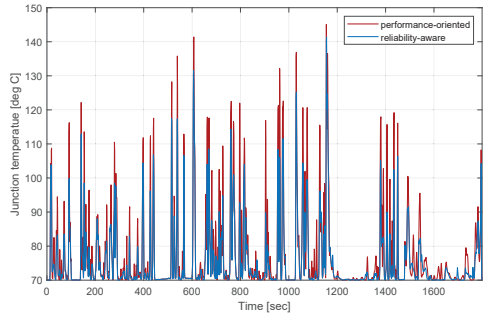

Fig. 6. Representation of the SiC MOSFET junction temperature variation, with a particular focus on relevant segments.

References

[1] M. Fanoro, M. Božanić, and S. Sinha, "A Review of the Impact of Battery Degradation on Energy Management Systems with a Special Emphasis on Electric Vehicles," 2022.

[2] F. Spaven, Y. Liu, and M. Baghdadi, "Going further with smaller EVs: System-level battery range, emissions and charging infrastructure analysis," *Journal of Cleaner Production*, vol. 369, 2022.

[3] D. Pevec, J. Babic, A. Carvalho, Y. Ghiassi-Farrokhfal, W. Ketter, and V. Podobnik, "A survey-based assessment of how existing and potential electric vehicle owners perceive range anxiety," *Journal of Cleaner Production*, vol. 276, 2020.

[4] K. Sato, D. Navarro, S. Sekizaki, Y. Zoka, N. Yorino, H. J. Mattausch, and M. Miura-Mattausch, "Prediction of DC-AC converter efficiency degradation due to device aging using a compact MOSFET-aging model," *IEICE Transactions on Electronics*, vol. E103.C, no. 3, pp. 119–126, 3 2020.

[5] S. Sudhakar, V. Sze, and S. Karaman, "Data Centers on Wheels: Emissions From Computing Onboard Autonomous Vehicles," *IEEE Micro*, vol. 43, no. 1, 2023.

[6] G. Zardini, N. Lanzetti, M. Pavone, and E. Frazzoli, "Analysis and Control of Autonomous Mobility-on-Demand Systems," *Annual Review of Control, Robotics, and Autonomous Systems*, vol. 5, no. 1, pp. 633–658, 6 2022.

[7] J. Zhang, T. Liu, and J. Qiao, "Solving a reliability-performance balancing problem for control systems with degrading actuators under model predictive control framework," *Journal of the Franklin Institute*, vol. 359, no. 9, pp. 4260–4287, 2022.

[8] N. Requate and T. Meyer, "Active control of the reliability of wind turbines," *IFAC-PapersOnLine*, vol. 53, no. 2, pp. 12 789–12 796, 2020, 21st IFAC World Congress.

[9] Y. Ma, T. Chantem, R. P. Dick, and X. S. Hu, "Improving system-level lifetime reliability of multicore soft real-time systems," *IEEE Transactions on Very Large Scale Integration (VLSI) Systems*, vol. 25, no. 6, pp. 1895–1905, 2017.

[10] A. Rezaeizadeh, G. Zardini, S. Mastellone, A. Censi, and E. Frazzoli, "Reliability-aware control of power converters in mobility applications," in *2024 European Control Conference (ECC)*, 2024.

[11] Q. Huang, Q. Huang, H. Guo, and J. Cao, "Design and research of permanent magnet synchronous motor controller for electric vehicle," *Energy Science & Engineering*, vol. 11, no. 1, pp. 112–126, 2023.

[12] S. Yang, A. Bryant, P. Mawby, D. Xiang, L. Ran, and P. Tavner, "An industry-based survey of reliability in power electronic converters," in *2009 IEEE Energy Conversion Congress and Exposition*, 2009, pp. 3151–3157.

[13] U. D. of Defense, Ed., *The Military Handbook for Reliability Prediction of Electronic Equipment MIL-HDBK-217F*. Defense Printing Service, 1995.

[14] H. Wang, M. Liserre, F. Blaabjerg, P. de Place Rimmen, J. B. Jacobsen, T. Kvisgaard, and J. Landkildehus, "Transitioning to physics-of-failure as a reliability driver in power electronics," *IEEE Journal of Emerging and Selected Topics in Power Electronics*, vol. 2, no. 1, pp. 97–114, 2014.

[15] M. Ciappa and W. Fichtner, "Lifetime prediction of igbt modules for traction applications," in *2000 IEEE International Reliability Physics Symposium Proceedings*, 2000, pp. 210–216.

[16] U. S. Arendt Wintrich, "Power cycle model for igbt product lines," August 2021.

[17] A. Czechowski and A. Lenk, "Miner's rule in mechanical tests of electronic parts," *IEEE Transactions on Reliability*, vol. R-27, no. 3, pp. 183–190, 1978.

[18] E. ASTM *et al.*, "Standard practices for cycle counting in fatigue analysis," *Standard Practices for Cycle Counting in Fatigue Analysis*, 2011.

[19] D. Benasciutti, A. Cristofori, and R. Tovo, "Analogies between spectral methods and multiaxial criteria in fatigue damage evaluation," *Probabilistic Engineering Mechanics*, vol. 31, pp. 39–45, 2013.

[20] C. E. Larsen and T. Irvine, "A review of spectral methods for variable amplitude fatigue prediction and new results," *Procedia Engineering*, vol. 101, pp. 243–250, 2015.

[21] J. Mattingley and S. Boyd, "CVXGEN: A code generator for embedded convex optimization," *Optimization and Engineering*, vol. 12, no. 1, pp. 1–27, 2012.